Check for updates

Low-temperature magnetic properties of deeply buried gas hydrate bearing sediments: a case study from IODP expedition 375 site U1519C in the Hikurangi subduction zone, New Zealand

Shixian Liu, Xuesen Li* and Kunyu Xu

College of Earth Sciences, Guilin University of Technology, Guilin, China

The diagenetic pathways, mineral types, and products of magnetic minerals in gas hydrate-bearing sediments are closely linked to burial depth. During IODP Expedition 375, drilling at the northern Hikurangi margin recovered 83.09 m of core from the gas hydrate stability zone (518.4−640.0 m depth) at Site U1519C. This provides an exceptional opportunity to investigate progressive diagenesis and fluid-driven late-stage diagenesis in deeply buried gas hydrate-bearing sediments. We conducted low-temperature magnetic measurements on 13 samples from this interval, including: (i) Low-temperature cycling (LTC) cycles, (ii) Zero-field-cooled (ZFC) and field-cooled (FC) curves, (iii) Low-temperature hysteresis loops, and (iv) Low-temperature alternating current (AC) magnetic susceptibility. Using features such as low-temperature transitions and curve trajectory patterns, we determined the types, concentrations, and assemblages of magnetic minerals, analyzed the origins of magnetic particles. Key results reveal: (1) Deeply buried sediments exhibit notably low SIRM intensity, indicating scarce magnetic minerals dominated by superparamagnetic (SP) and single-domain (SD) particles. This indicates that the deeply buried sediments experienced extensive pyritization under sustained reducing diagenetic conditions; (2)Despite the dominance of SP signals in the low-temperature FC/ZFC curves, the observation of the Verwey transition at ~118 K—a characteristic low-temperature phase transition stemming from magnetite's structural transformation—provides definitive evidence for the presence of trace magnetite even at such depths (>580 mbsf); (3) A double Verwey transition (~106 K and ~118 K) was observed in some samples, which indicates the coexistence of biogenic magnetite and nearly stoichiometric magnetite; (4) Authigenic Greigite (Fe_3S_4), an intermediate product of pyritization (FeS_2), is detected. Some greigite likely exists as SP particles, while a low index of hysteresis parameters (D_{JH}) indicates limited contributions from stable SD greigite among ferrimagnetic minerals.This study provides low-temperature magnetic evidence for diagenetic processes affecting magnetic minerals in deeply buried gas hydrate-bearing sediments. It reveals partial magnetite preservation, greigite formation and transformation, and

ultimate pyritization, offering new insights into magnetic mineral evolution in such environments.

1 Introduction

Gas hydrates are solid crystalline compounds formed when gas (primarily methane) and water combine under high-pressure and low-temperature conditions. Authigenic magnetic iron sulfides in marine sediments are strongly associated with gas hydrate occurrence. Moreover, their presence may represent a key indicator for identifying hydrate-bearing zones. Numerous studies have investigated magnetic mineral variations in shallow sediments from gas hydrate-bearing zones. Housen and Musgrave (1996) conducted detailed rock magnetic analyses on cores from ODP Leg 146 Sites 892 and 889/890 along the Cascadia margin. This work showed that hydrate-bearing sediments primarily contain fine-grained magnetic iron sulfides, whereas sediments adjacent to the upper and lower boundaries of the gas hydrate-bearing intervals contain mixtures of magnetite and iron sulfides. Larrasoaña et al. (2007) combined detailed mineral magnetic analyses and electron microscopy observations on gas hydrate-bearing sediments from ODP Leg 204 Sites 1244 and 1252. This work revealed micrometer-scale authigenic greigite and monoclinic pyrrhotite as the primary magnetic carriers in hydrate-bearing intervals. Within sulfide zones, anaerobic oxidation of methane (AOM) zones, and methane hydrate stability zones, these magnetic iron sulfides form as byproducts of microbially mediated reductive diagenesis. Kars and Kodama (2015) conducted a high-resolution rock magnetic study on 218 Pleistocene sediment samples from 70 to 110 m below seafloor (mbsf) in Hole C0008C, IODP Expedition 316, Nankai Trough. This work revealed three magnetic mineral assemblages: magnetite, greigite-pyrrhotite, and their mixtures. Sediments carrying the authigenic greigite-pyrrhotite assemblage were associated with gas hydrate occurrences. This study demonstrated the feasibility of using rock magnetic parameters to rapidly detect and quantify hydrate-related authigenic iron sulfides. In addition, the rock magnetic properties of sediments in gas hydrate-dominated systems have been extensively investigated using magnetic methods to understand the diagenesis of magnetic minerals, as reported in areas such as the Sea of Marmara (Yang et al., 2023) and the Bay of Bengal (Gaikwad et al., 2021; Gaikwad et al., 2022; Badesab et al., 2020). Collectively, these pioneering studies demonstrate that biogeochemical processes associated with gas hydrate formation generate authigenic magnetic iron sulfides with distinct, detectable magnetic signatures. Yet magnetic mineral evolution in deeply buried systems remains enigmatic. Increasing burial depth elevates geothermal gradients and enhances fluid flux, transitioning early reductive diagenesis in shallow sediments to progressive and fluid-driven late-stage diagenesis in intermediate-to-deep strata. This raises a critical question: How do diagenetic authigenic magnetic sulfides associated with gas hydrate occurrence evolve in shallow sediments? Two potential evolutionary pathways emerge: (1) During late diagenesis, hydrate formation at the base of sulfate reduction zones restricts

H_2S concentration and pore-water exchange. This inhibits complete pyritization, favoring preservation and continued growth of authigenic greigite-monoclinic pyrrhotite from earlier diagenetic iron sulfides. (2) Alternatively, sustained microbial activity fueled by hydrates could supply continuous H_2S, dissolving earlier iron sulfides and driving complete conversion to paramagnetic pyrite with minor residual ferrimagnetic oxides. Determining the dominant pathway requires further investigation.

Low-temperature magnetism offers distinct advantages for detecting magnetic carriers in weakly magnetic sediments. With high sensitivity (10^{-9} emu), minimal thermal noise, and reduced electromagnetic interference, it excels at identifying biogenic single-domain magnetite (Moskowitz et al., 1993). Biogenic magnetite forms through synthesis by magnetotactic bacteria, microorganisms commonly found in reducing sediments and porewaters with high concentration of hydrogen sulfide (H_2S) (Bazylinski et al., 1991). Remanence measurements during temperature cycling reveal key magnetic mineral characteristics—including mineral species, grain size distribution, and oxidation state—providing insights into their origin and diagenetic history (Smirnov and Tarduno, 2000; Chang et al., 2013). Roberts et al. (2011) applied low-temperature magnetometry to tectonically uplifted sediment samples from the Neogene marine sequence of the Hikurangi Margin. The authors identified a monotonic and rapid decrease in saturation remanence between 0 and 50 K in the zero-field-cooled (ZFC) and field-cooled (FC) curves and demonstrated that it was caused by superparamagnetic (SP) greigite. Applying low-temperature magnetic methods to hydrate-bearing sediments (0–492 mbsf) at IODP Site U1518, Kars et al. (2021) precisely identified magnetite and found indirect evidence for greigite. They further demonstrated how rock magnetic parameters can rapidly quantify key properties of authigenic iron sulfides—including concentration and grain size—in hydrate-associated sediments.

During IODP Expedition 375 at the northern Hikurangi margin, drilling at Site U1519C recovered Miocene turbiditic silts from 518.4 to 640 mbsf. We characterized the magnetic mineralogy and grain-size distribution of the deeply buried gas hydrate stability zone by conducting the first systematic low-temperature magnetic measurements on 13 samples. The methodology comprised (i) low-temperature cycling (LTC) cycles, (ii) ZFC and FC curves, (iii) low-temperature hysteresis loops, and (iv) low-temperature alternating current (AC) susceptibility. All measurements were conducted following standard low-temperature rock magnetic protocols. These analyses were performed using a Quantum Design MPMS XL-7 magnetometer at the Paleomagnetic and Rock Magnetic Laboratory of the University of Bremen, Germany. By integrating diagnostic features such as low-temperature transitions and curve trajectories, this study aims to identify magnetic mineral assemblages and their unique "magnetic fingerprints". This study establishes the physical foundation for magnetic identification of hydrate-bearing

strata and core magnetic logging techniques. Furthermore, these fingerprints, when preserved from paleo-gas hydrate activity, can serve as a scientific basis for recognizing fossil gas hydrate zones—sedimentary layers formed by the dissociation of ancient gas hydrate.

1.1 Study area

The Hikurangi subduction zone, situated in the South Pacific Ocean east of New Zealand (Figure 1A), features westward subduction of the Pacific Plate beneath the Australian Plate along the Hikurangi Trench at 4.5–5.5 cm/yr (Barnes and Wu, 2019). The subducting Pacific Plate comprises the Hikurangi Plateau—a Cretaceous oceanic plateau dominated by mafic-ultramafic rocks—overlain by ~1 km of Mesozoic-Cenozoic sedimentary cover. The northern margin hosts multiple seamounts on the subducting plate, creating an irregular subduction interface with localized frontal tectonic erosion features associated with seamount subduction.

IODP Expedition 375 (8 March - 5 May 2018) investigated slow-slip earthquakes through drilling operations at the northern Hikurangi margin. The study employed core sampling, and long-term borehole monitoring to characterize hydrogeological, geochemical, and physical processes. Drilling to 650 mbsf at Site U1519 revealed three major unconformity-bounded lithostratigraphic units (Table 1). Integrated shipboard analyses—including infrared thermal imaging of cores, porewater chloride measurements, bottom-simulating reflector (BSR) identification (Figure 1B)—confirmed the gas hydrate stability zone within the Miocene turbiditic silts (518.4–640.0 mbsf). Centimeter-scale hydrate layers were encountered at 587.25–587.32, 605.74–605.93, and 617.15–617.20 mbsf. Below the sulfate-methane transition zone (SMTZ), hydrates exhibit low saturation (<10%) and heterogeneous distribution patterns.

At Site U1519, the Late to Middle Pleistocene section (from 4.40 to 536.32 mbsf) is characterized by a high sedimentation rate of 0.84 m/ky, indicating rapid deposition (Barnes and Wu, 2019). Recent research in the Bay of Bengal has also reported that high sediment accumulation rates facilitate the rapid burial and preservation of detrital magnetic grains shortly after their deposition (Badesab et al., 2019; Badesab et al., 2022). In contrast, the age of the lower section (below 536.32 mbsf) is poorly constrained, and its sedimentation rate remains uncertain. Therefore, it remains unclear whether the magnetic minerals in the study area's sediments are favorably influenced by rapid sedimentation for their preservation.

2 Materials and methods

2.1 Experimental overview

In this study, a suite of low-temperature magnetic measurements was employed to characterize the magnetic mineralogy of the sediment samples. These measurements include LTC cycles, FC/ZFC remanence, AC susceptibility, and low-temperature hysteresis

experiments. This section briefly outlines the experimental procedures underpinning each technique. The interpretation of these measurements allows for the identification of magnetic phases (e.g., magnetite, greigite) and their domain states, which is crucial for understanding the magnetic signal recorded in the geological record.

2.2 Site description and drilling generalities

Drilling at Site U1519 employed both the Rotary Core Barrel (RCB) system for discrete intervals (108–163.6, 250–288.4, and 520–640 mbsf in Hole U1519C) and the Advanced Piston Corer (APC) system which continuously cored from seafloor to 85.8 mbsf in Holes U1519D and U1519E. Thirteen sediment core samples were collected from the 587–618 mbsf interval in Hole U1519C (Table 2).

2.3 Low-temperature magnetic measurements

Low-temperature rock magnetic experiments, including FC, ZFC, and LTC measurements, were conducted on all thirteen sediment core samples from the 587–618 mbsf interval in Hole U1519C. All measurements employed a Quantum Design MPMS XL-7 magnetometer at the University of Bremen's Paleomagnetism Laboratory.

For the FC measurements, samples were cooled from 300 K to 5 K in a 5 T field to impart a saturation isothermal remanent magnetization (SIRM), after which the remanence was recorded during zero-field warming to 300 K. For the ZFC protocol, samples were first cooled to 5 K in zero field, then subjected to a 5 T pulse to impart a SIRM, with remanence subsequently measured during warming in zero field. The LTC procedure involved magnetizing samples at 300 K in a 5 T field, cooling them to 5 K in zero field, and then measuring remanence during stepwise warming to 300 K in 2 K increments.

A subset of nine samples was selected for further analysis. AC susceptibility was measured on this subset at frequencies of 1, 10, and 111 Hz during warming after zero-field cooling to 5 K. Hysteresis loops were also acquired for the same nine samples at temperatures of 5, 70, 130, and 300 K by sweeping the magnetic field between ±1 T.

2.4 Shipboard data

Onboard measurements provided magnetic susceptibility (MS) and porewater geochemical data (Figure 2). Within the sampled interval (570–620 mbsf), MS values are consistently low (0–30 × 10^{-5} SI; Figure 2). No systematic depth-dependent trends were observed in porewater chemistry or MS. Discrete anomalies occur locally, most notably at 605–606 mbsf showing concurrent increases in MS, chloride (Cl^-), and methane (CH_4), alongside decreased sulfate (SO_4^{2-}) concentrations.
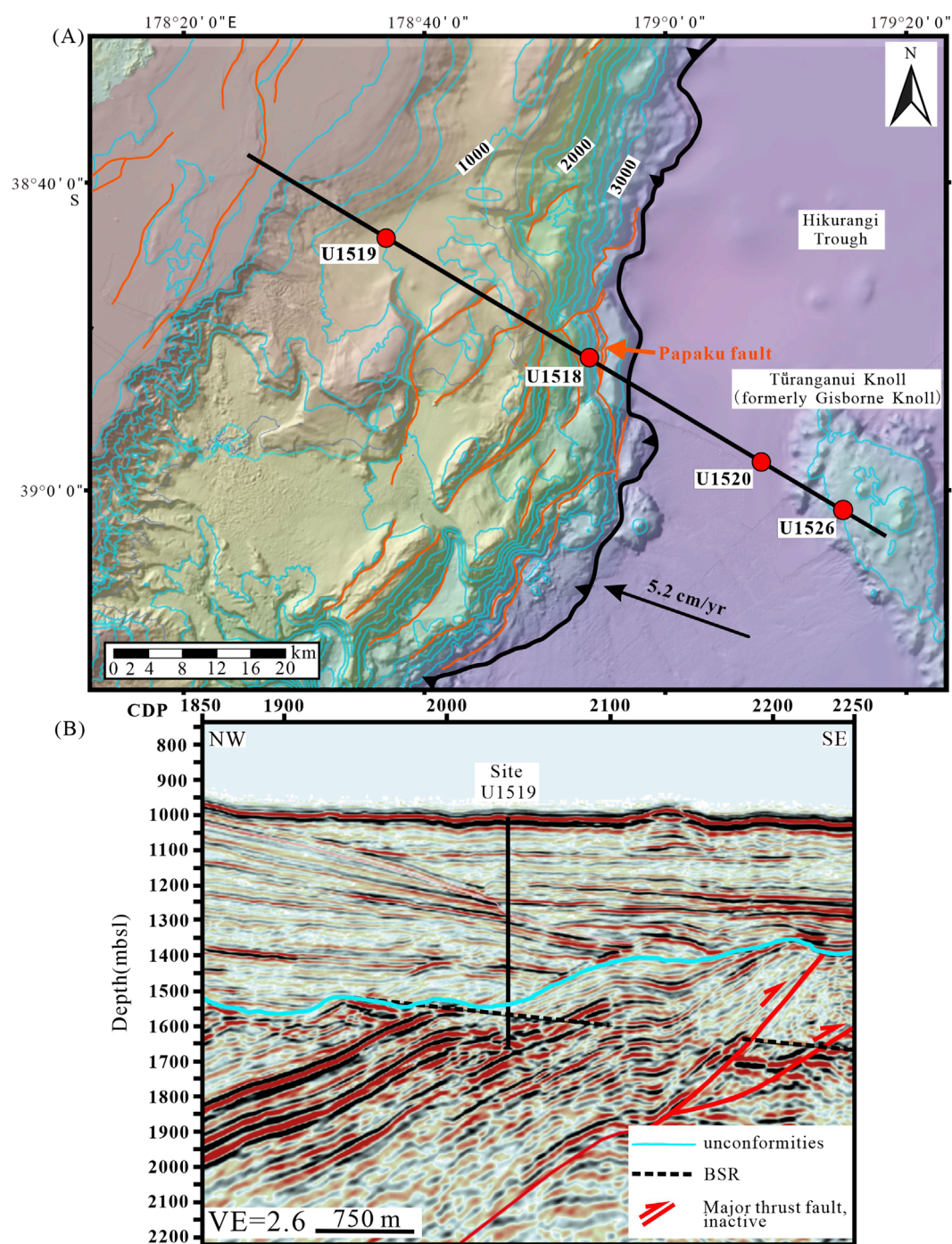
FIGURE 1
(A) Bathymetry map showing seismic line 05 CM-04 (black) and IODP Expedition 375 drilling locations (red circles) off the East Coast of New Zealand's North Island. Drilling targeted tectonic elements: the Papaku thrust fault at the accretionary wedge front (Site U1518), the forearc Tuaheni Basin (Site U1519), the leading edge of the subducting Turangahui Knoll (Site U1520), and its summit (Site U1526). Site U1519 is situated on the upper continental slope of the Hikurangi margin, ~38 km offshore at ~1000 m water depth within the landward portion of the mid-slope Tuaheni Basin. Modified from Saffer et al. (2019). **(B)** Interpreted seismic profile along line 05 CM-04 at Site U1519. VE = vertical exaggeration. Modified from Barnes et al. (2019).

3 Result

3.1 Low-temperature SIRM warming

Figure 3 presents low-temperature SIRM warming results for samples from site U1519C captured in this Expedition following FC and ZFC treatments. The FC curve consistently lies slightly above the ZFC curve (Figures 3A–C), indicating the absence of multi-domain (MD) magnetite (Housen and Moskowitz, 2006). Below 50 K, all curves exhibit rapid decay, characteristic of magnetic responses from SP particles (Tarduno, 1995). First-derivative analysis (10–40 K) reveals no significant peaks during warming.

TABLE 1 Summary of lithostratigraphic units encountered at Site U1519.

Unit	Depth (mbsf)	Approximate thickness (m)	Lithology and description	Depositional settin	Structural attitudeg
1	~0 - 260/270	~260–270	Horizontally stratified basin fill consisting of turbidite sequences	Basin floor	Horizontal
2	~260/270 - 530	~260–270	A slope sequence of stratified sediments	Slope	Southeast-dipping
3	~120	~120	Northwest-dipping unit in the hanging wall of an inactive thrust fault	Basal unit (structural)	Northwest-dipping

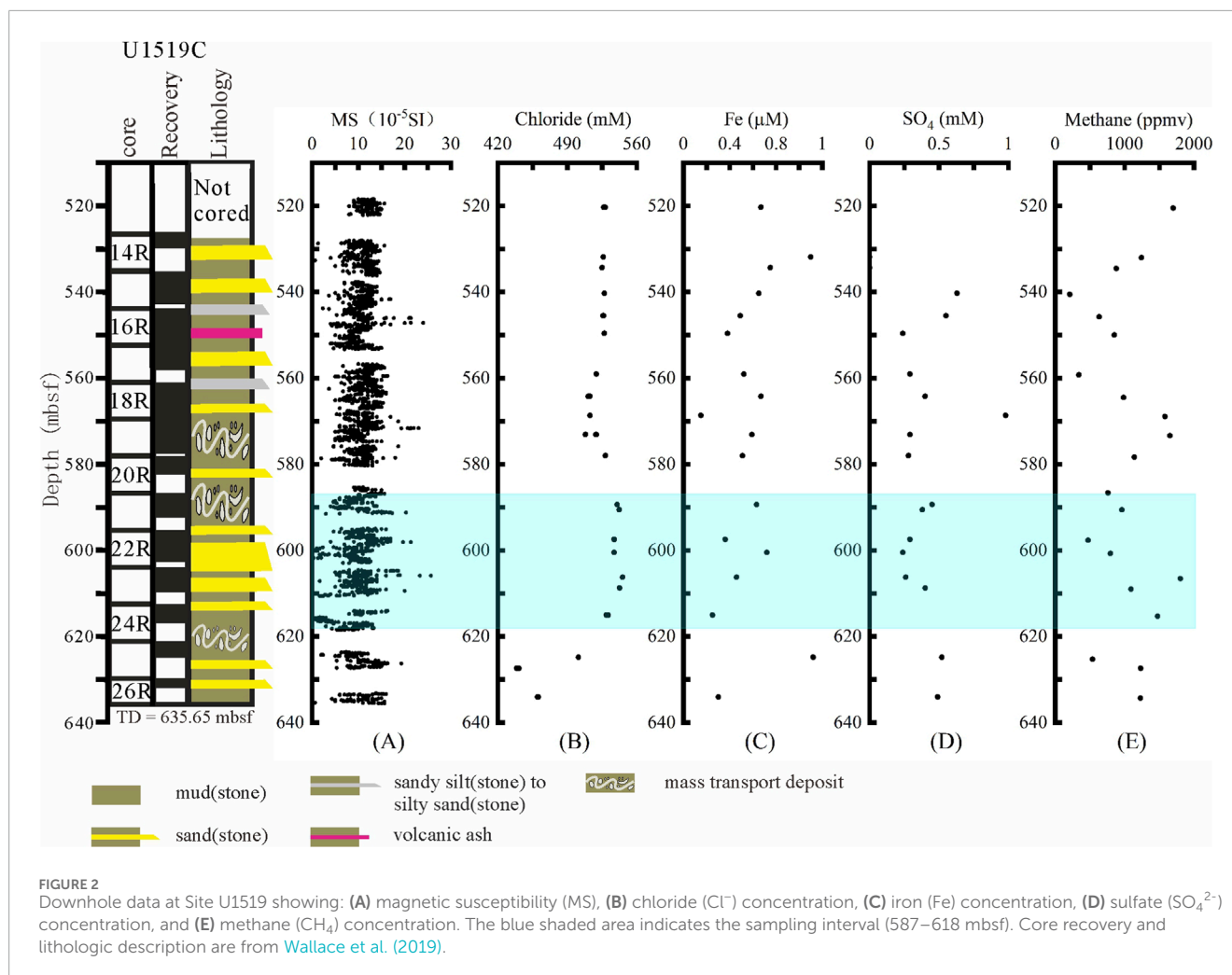TABLE 2 Rock magnetic parameters of samples from different depths.

	Depth (mbsf)	Lithology	δ_{FC}/δ_{ZFC}	F_{SP}	Mr/Ms	Bcr/Bc	D_{JH}
CUBE9497451	587.1	Mudstone	1.027	0.981	0.188	3.333	0.0565
CUBE9497461	587.13	Mudstone	1.031	0.968	0.182	4.029	0.0452
WDGE9497641	587.32	Sandstone	1.03	0.983	—	—	—
CUBE9497471	587.33	Sandstone	1.055	0.984	—	—	—
CUBE9503351	605.48	Mudstone	1.03	0.985	0.176	3.291	0.0533
CUBE9503371	605.74	Sandstone	1.005	0.962	0.207	3.859	0.0537
CUBE9503381	605.8	Sandstone	1.034	0.946	0.257	2.711	0.0948
WDGE9503551	605.8	Sandstone	1.003	0.960	0.25	3.294	0.0759
CUBE9503391	605.96	Mudstone	1.026	0.992	0.18	4.08	0.0442
CUBE9504481	617.04	Mudstone	1.038	0.977	—	—	—
WDGE9507191	617.1	Mudstone	1.033	0.993	0.139	4.685	0.0296
CUBE9504501	617.17	Mudstone	1.025	0.99	—	—	—
CUBE9504521	617.32	Mudstone	1.027	0.986	0.099	7.231	0.0137

"—" denotes unmeasured data points.

This absence of phase transitions precludes pyrrhotite (~34 K) and siderite (~37 K) within the 30–40 K interval (Frederichs et al., 2003). Convergence of ZFC and FC curves at ~50 K (Figures 3A–C) may reflect Ti impurities in magnetite (Wang et al., 2021). Remanence losses exceeding 90% during warming confirm SP particles dominate the SIRM signal. No distinct transitions appear in raw FC/ZFC curves, including features characteristic of greigite. First-derivative magnification reveals subtle Verwey transitions at ~106 K and ~118 K (Figure 3D), indicating coexisting biogenic magnetite (~106 K) and near-stoichiometric magnetite (~118 K) (Chang et al., 2016a). Furthermore, the FC/ZFC curves coincide beyond the Verwey transition at 118 K, suggesting the absence of goethite; no evidence of the Morin transition (characteristic of hematite) was observed near 260 K (Liu et al., 2006).

3.2 Low-temperature cycling of RTSIRM

LTC results reveal distinct magnetic behaviors. At 587.13 mbsf (Figure 4A), the LTC warming and cooling branches separate at ~110 K, with no distinct Verwey transition. The relatively low remanence loss of ~9% over the entire cycle indicates the presence of fine-grained, nanoscale magnetite particles (Özdemir et al., 2002). Upon cooling from room temperature (300 K) to 5 K, the remanence increased by a factor of 2.4. Subsequently, during warming from 5 K, the remanence decreased rapidly by ~50% between 5 K and 50 K. The LTC behavior differed within the discrete anomaly zone (~605 mbsf). Sample CUBE9503381 (Figure 4A) displayed more than double the SIRM intensity of the other two samples and exhibited reduced remanence decay between 5 K and 40 K. The warming and cooling curves separated above 100 K. A distinct hump

FIGURE 2
Downhole data at Site U1519 showing: **(A)** magnetic susceptibility (MS), **(B)** chloride (Cl⁻) concentration, **(C)** iron (Fe) concentration, **(D)** sulfate (SO₄²⁻) concentration, and **(E)** methane (CH₄) concentration. The blue shaded area indicates the sampling interval (587–618 mbsf). Core recovery and lithologic description are from Wallace et al. (2019).

appeared in the cooling curve between 150 K and 200 K, which was absent in the warming curve. This pattern is characteristic of nearly stoichiometric, SD magnetite grains (Özdemir et al., 2002). In contrast, according to Özdemir and Dunlop (2010), partially oxidized magnetite exhibits an irreversible hump in both cooling and warming cycles within the 150–200 K range. The overall remanence loss over the full LTC cycle was higher here, reaching ~13%, consistent with the presence of coarser magnetite grains. Collectively, the LTC data indicate that samples from the main study area contain minor amounts of fine-grained SD magnetite. A significantly higher content of sub-micron single-domain (SD) magnetite were found exclusively within the discrete anomaly zone (~605 mbsf).

3.3 Low-temperature AC susceptibility

AC magnetic susceptibility decreased rapidly and monotonically during warming for all samples, showing no discernible peaks (Figures 4D–F), confirming paramagnetic dominance through its characteristic temperature dependence and negligible ferromagnetic contribution. The in-phase susceptibility (χ') exhibited pronounced temperature dependence across all measured frequencies (1, 10,

and 111 Hz), decreasing by >90%. Crucially, χ' displayed no frequency dependence, consistent with paramagnetic mineralogy (e.g., pyrite). As temperature increases, susceptibility gradually diverges at different frequencies. As proposed by Chang et al. (2013), this behavior occurs as some SD particles become gradually unblocked and exhibit SP behavior with increasing temperature. This effect was most pronounced in the 605.8 mbsf sample (Figure 4E). The frequency dependence of magnetic susceptibility, as determined by the frequency-dependent parameter ($\chi_{df}(\%)$), was calculated using Equation 1:

$$\chi_{df}(\%)\left(= 100 \times \left(\chi_{lf} - \chi_{hf}\right)/\chi_{lf}\right) \tag{1}$$

For sample CUBE-9503381, measurements show $\chi_{df}(\%)$ values of approximately 10% at 1–10 Hz frequencies, reaching ~13% when comparing 1 Hz–111 Hz. These elevated values indicate significant concentrations of SP magnetic minerals (Kars et al., 2018).

3.4 Hysteresis loops

Prior to high-field slope correction, hysteresis loops exhibited negligible opening at low fields (Figures 4G–I), except for those
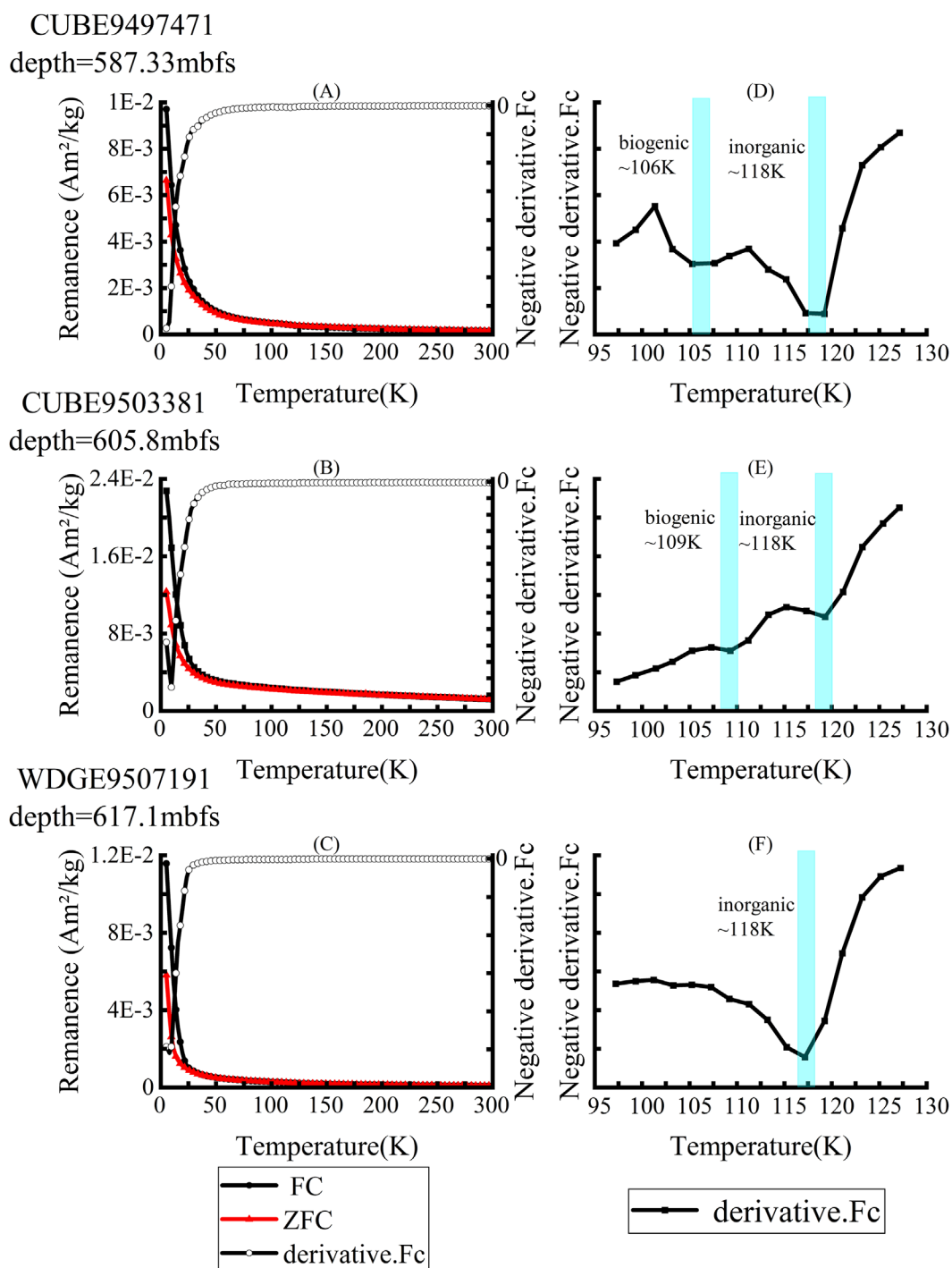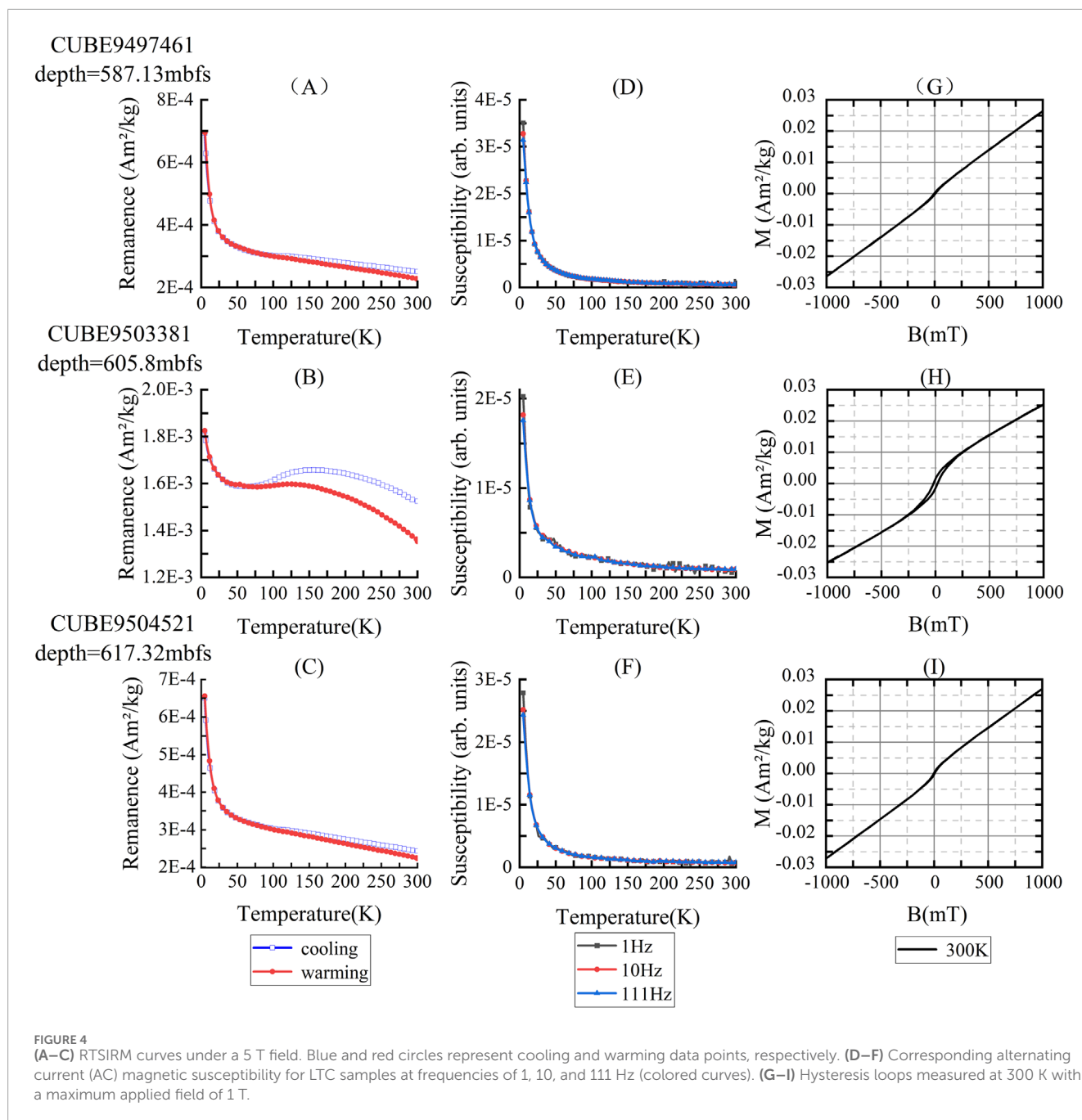
FIGURE 3
Representative rock magnetic measurements: FC/ZFC curves for samples from Expedition U1519. **(A−C)** FC/ZFC curves and the first derivative of the FC curve. **(D−F)** Close-up view of the first derivative of the FC curve within the 95−130 K range. The blue shaded region highlights the peak corresponding to the Verwey transition, diagnostic of both biogenic and inorganic magnetite.

within the discrete anomaly zone. Central loop width increased systematically with temperature (Figures 5A–D), confirming paramagnetic dominance consistent with AC susceptibility results (Wang et al., 2020). The enhanced paramagnetic signatures within the reducing gas hydrate stability zone are ascribed to pyrite formation through reductive dissolution and sulfidation of magnetite. The temperature-dependent variation of magnetization follows paramagnetic behavior, further confirming

FIGURE 4
(A–C) RTSIRM curves under a 5 T field. Blue and red circles represent cooling and warming data points, respectively. **(D–F)** Corresponding alternating current (AC) magnetic susceptibility for LTC samples at frequencies of 1, 10, and 111 Hz (colored curves). **(G–I)** Hysteresis loops measured at 300 K with a maximum applied field of 1 T.

the predominance of paramagnetic minerals. The paramagnetic magnetization (M_p), as described by Curie's law, was calculated using Equation 2:

$$M_p(B, T) = \frac{CB}{u_0 T} \tag{2}$$

where C is the Curie constant and μ_0 is the vacuum permeability (Paterson et al., 2018). When cooling from 130 K to 70 K, the uncorrected maximum magnetization increased by a factor of 1.92 (Figures 5B,C). The excess enhancement

beyond theoretical predictions likely stems from magnetite's Verwey transition near 118 K amplifying magnetization effects.

Most samples plot within the pseudo-single-domain (PSD) region on the Day-plot (Figure 6). This apparent distribution may reflect a known limitation of Day-plots: mixtures of SD and SP grains can artifactually shift data into the pseudo-single-domain (PSD) region (Tauxe et al., 2002; Pick and Tauxe, 1994). The data trend parallels theoretical SD + SP mixing curves, indicating that magnetic minerals exist predominantly as mixtures of SD and SP particles.
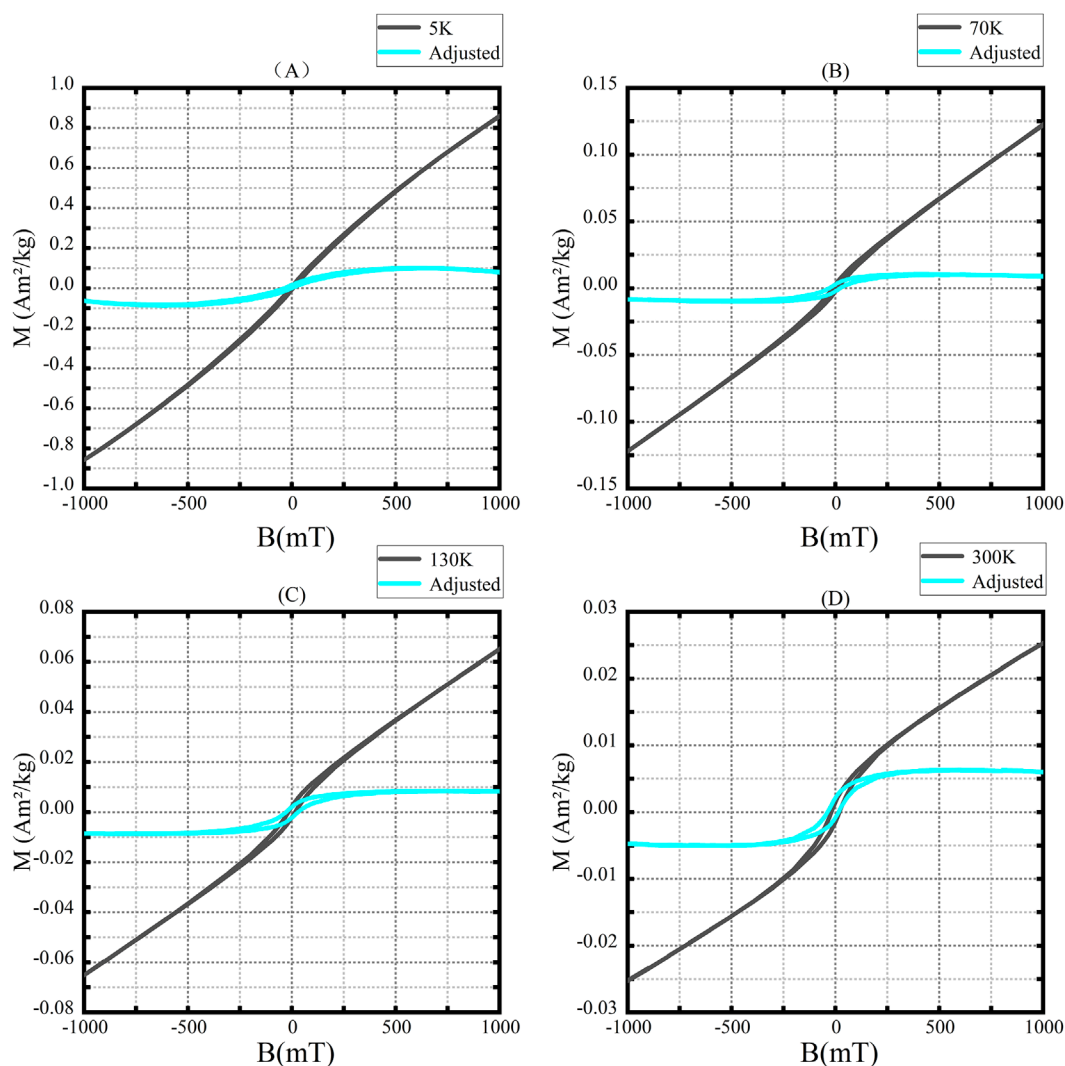
FIGURE 5
Hysteresis loops for sample CUBE9503381 at 605.8 mbsf under a 1 T applied field, showing raw and slope-corrected data at **(A)** 5 K, **(B)** 70 K, **(C)** 130 K, and **(D)** 300 K.
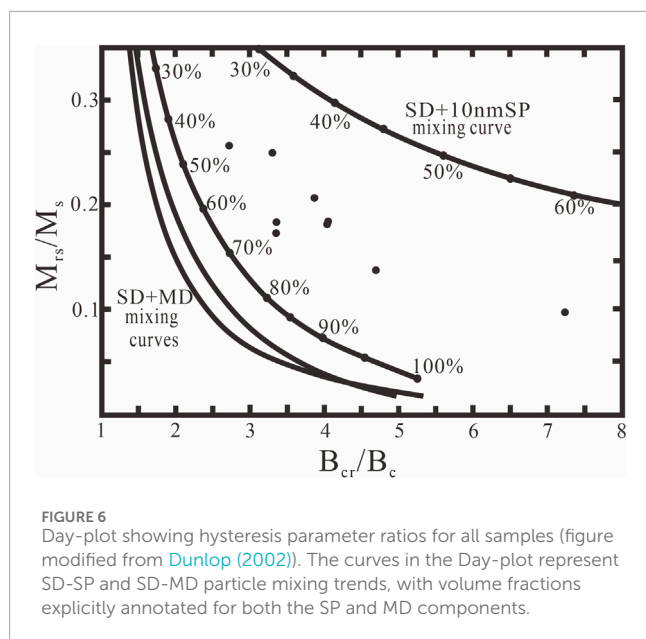
The proportion of SP particles shows an increasing trend with depth.

4 Discussion

4.1 Magnetite preservation mechanisms in deep gas hydrate systems

Site U1519, situated on the upper continental slope of the Hikurangi Margin, represents a sulfate-reducing setting where microbially produced hydrogen sulfide (H_2S) reacts with iron phases to 7s that contributes to extensive magnetite depletion in sulfidic marine sediments (Chang et al., 2016a). However, our low-temperature measurements reveal that deeply buried marine sediments below 580 mbsf show that while hysteresis loops and AC susceptibility curves both indicate dominant paramagnetic pyrite signatures, detectable Verwey transitions in first-derivative

FC curves confirm persistent minor magnetite preservation. The surviving magnetite consists of nearly stoichiometric sub-micron particles. Day-plot analysis confirms these SD grains coexist with SP minerals (Figure 6). This suggests that preserved magnetite grains in deeply buried samples likely exist as a broad distribution of nanoscale particles. Although fine-grained magnetite typically undergoes preferential dissolution in deep-sea reducing environments, analyses of samples from Cretaceous seafloor basalts, mid-ocean ridge basalts, and the Oman margin (NW Arabian Sea) reveal that silicate-hosted magnetite inclusions provide effective physical protection against dissolution (Chang et al., 2016a; Pick and Tauxe, 1994; Smith, 1979). Chang et al. (2016b) identified signals indicative of magnetite inclusions within silicate particles in first-order reversal curve (FORC) diagrams of these samples. This confirms that silicate grains remain structurally stable in sulfide-rich environments, thereby protecting encapsulated magnetite from dissolution. Transmission electron microscopy (TEM) analysis

FIGURE 6
Day-plot showing hysteresis parameter ratios for all samples (figure modified from Dunlop (2002)). The curves in the Day-plot represent SD-SP and SD-MD particle mixing trends, with volume fractions explicitly annotated for both the SP and MD components.

further verifies biogenic magnetite within these samples (Figure 7). This inclusion mechanism accounts for the limited magnetite preservation observed below 580 mbsf.

4.2 Authigenic greigite preservation in deep-buried sediments

During the sulfate reduction stage, the transformation of iron oxides to pyrite proceeds through intermediate iron sulfide phases (Liu et al., 2014; Roberts et al., 2011). As documented by Larrasoaña et al. (2007) at two ODP Leg 204 sites on the Cascadia margin, gas hydrate-bearing sediments contain authigenic greigite and monoclinic pyrrhotite as the dominant magnetic carriers. Greigite preservation potential in deep sediments is well-documented and controlled by environmental parameters including methane concentration, dissolved Fe^{2+}, and sulfate availability (Kars et al., 2021; Roberts et al., 2011).

Low-temperature measurements on deep-seated samples (>580 mbsf) from IODP Expedition 375 Site U1519 reveal uniformly weak SIRM across all specimens (Figures 3A–C). All samples contained significant proportions of SP minerals, as evidenced by pronounced monotonic changes in low-temperature FC/ZFC and LTC measurements that substantially suppressed the Verwey transition (Figures 3, 4). The frequency-dependent susceptibility (F_{SP}) parameter, an estimator of SP magnetic mineral content, was calculated using Equation 3:

$$F_{SP} = \frac{(M_{rs}(5) - M_{rs}(300))}{M_{rs}(5)} \quad (3)$$

where Mrs(T) denotes the saturation remanent magnetization measured at temperature T during FC measurement (Kars et al., 2017). While residual fields in MPMS magnetometers may overestimate F_{SP} in weakly magnetic samples (Roberts, 1995), our measurements consistently show high SP fractions (F_{SP} >90%) in deep sediments (Table 2), confirming SP dominance.

The absence of a Verwey transition in SP magnetite at low temperatures, combined with greigite's lack of characteristic magnetic transitions, complicates the discrimination of SP particle sources. However, studies from the Hikurangi subduction zone and vicinity report authigenic greigite occurring as broadly distributed SP particles (Moskowitz et al., 1993; Qian et al., 2021). Rowan and Roberts (2006) identified authigenic greigite—formed during diagenesis through magnetite dissolution—in tectonically uplifted Neogene marine sediments from the Hikurangi margin (Qian et al., 2021), confirming abundant SP greigite within these deposits. Subsequently, our FC curves closely match those reported by Roberts et al. (2011) for the same region, demonstrating a monotonic rapid decrease in saturation remanence (SIRM) between 5 and 50 K. This behavior was conclusively attributed to SP greigite (Liu et al., 2014). Low sulfate concentrations further inhibit pyritization, promoting greigite preservation (Kars et al., 2021). Dominant paramagnetic pyrite signatures in low-temperature measurements indicate pervasive pyritization throughout the reducing environment of deeply buried sampling zones. Below 580 mbsf at Site U1519C, low sulfate concentrations and reactive iron concentrations (Figure 2) restrict microbial H_2S production. This likely arrested greigite-to-pyrite conversion near cessation, explaining authigenic greigite preservation. These conditions support greigite as partially source of the observed SP signatures in FC/ZFC curves.

The contribution of single-domain (SD) greigite to ferrimagnetic assemblages, as determined by the D_{JH} parameter (Kars et al., 2021), was calculated using Equation 4:

$$D_{JH} = \left(\frac{M_{rs}}{M_s}\right) / \left(\frac{B_{cr}}{M_c}\right) \quad (4)$$

Elevated D_{JH} values typically indicate substantial SD greigite fractions. Kars et al. (2021) reported that D_{JH} values typically fall below 0.2 in low-coercivity systems and exceed 0.3 in high-coercivity assemblages. Our low-coercivity samples exhibit depressed D_{JH} values ranging from 0.01 to 0.09. These low values indicate a diminished contribution of SD greigite within the ferrimagnetic mineral assemblage, consistent with dominant SP particle signatures. Isolated anomalously high values occur exclusively within the 605 mbsf interval, indicating an elevated proportion of authigenic greigite within the magnetic mineral assemblage. Greigite adopts a cubic spinel structure isostructural with magnetite, yet lacks distinctive low-temperature transitions analogous to magnetite's Verwey transition (Kars et al., 2017). Furthermore, the dominance of SP particles in samples suppresses magnetic contributions from other minerals, thereby constraining precise determination of their distribution characteristics solely through low-temperature magnetic methods.

4.3 Identification of biogenic magnetite

Rock samples from deep-burial zones exhibit two distinct Verwey transition peaks (~106 K and ~118 K) in first-derivative FC curves (Figure 4B). Following Chang et al. (2016a), these dual transitions indicate both biogenic magnetite and near-stoichiometric inorganic magnetite (Bazylinski et al., 1991). The ~118 K transition reflects near-stoichiometric composition, with
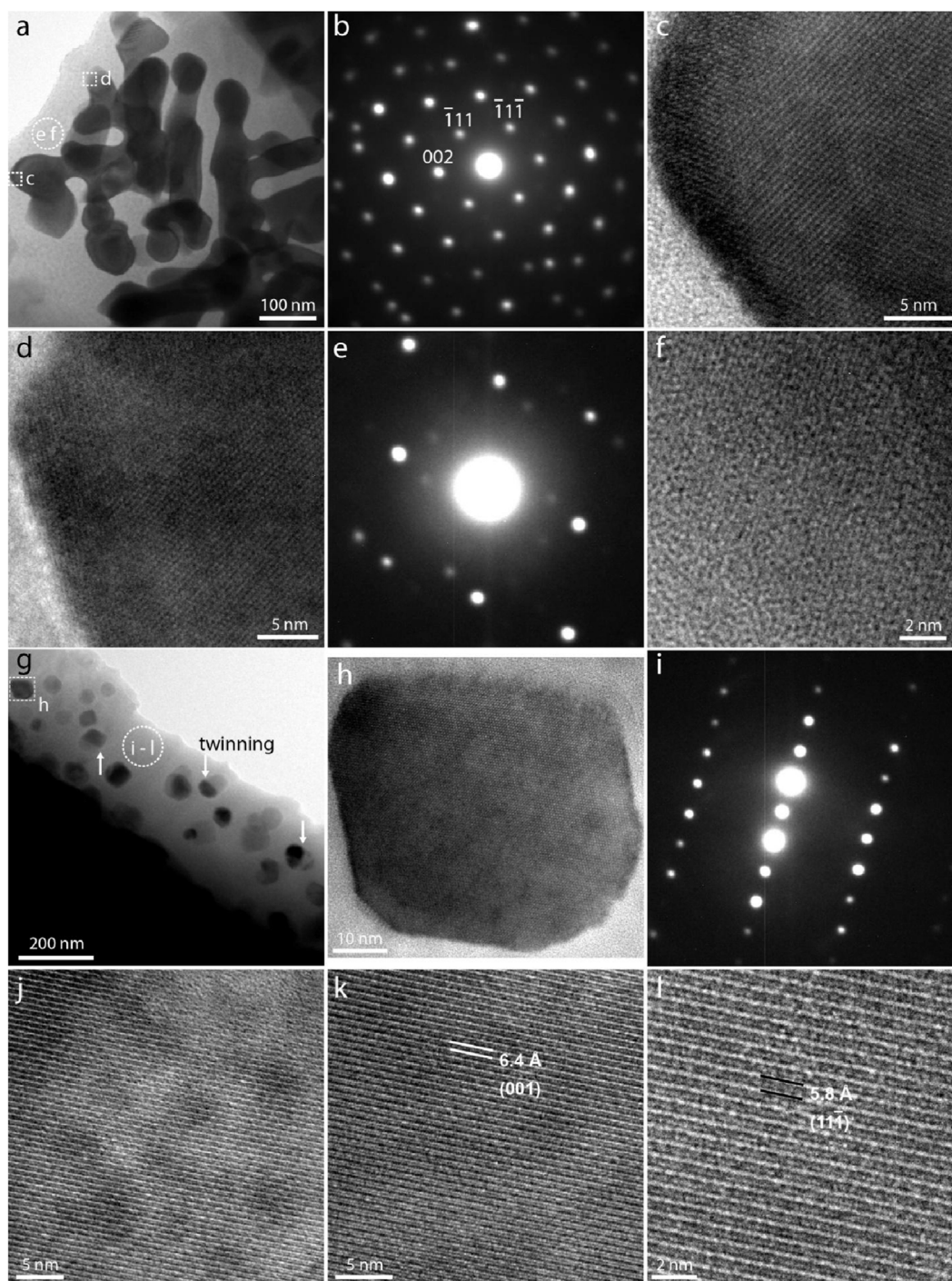
FIGURE 7
High-resolution TEM and SAED analyses of titanomagnetite inclusions within a plagioclase host mineral. **(a−l)** Results from two distinct areas in sample "MD01-2421-7-110". Images in **(b−d)** and **(h)** correspond to magnetic mineral (titanomagnetite) inclusions, while **(e,f)** and **(i−l)** correspond to the silicate host mineral (plagioclase). Clear lattice fringes for both phases are observed. Arrows in **(g)** indicate crystal twinning within a magnetic nanoparticle inclusion. Modified from Chang et al. (2016b).

deviations from the ideal ~120 K transition likely caused by impurities (e.g., Ti). Conversely, chain fragmentation or oxidation of magnetosomes can suppress the Verwey transition below 110 K (Chang et al., 2016a; Roberts et al., 2012), consistent with the ~106 K peak. As LTC tests revealed no oxidation features, we attribute the ~106 K peak to biogenic magnetite. The δ_{FC}/δ_{ZFC} ratio further discriminates biogenic magnetite and was calculated using Equation 5:
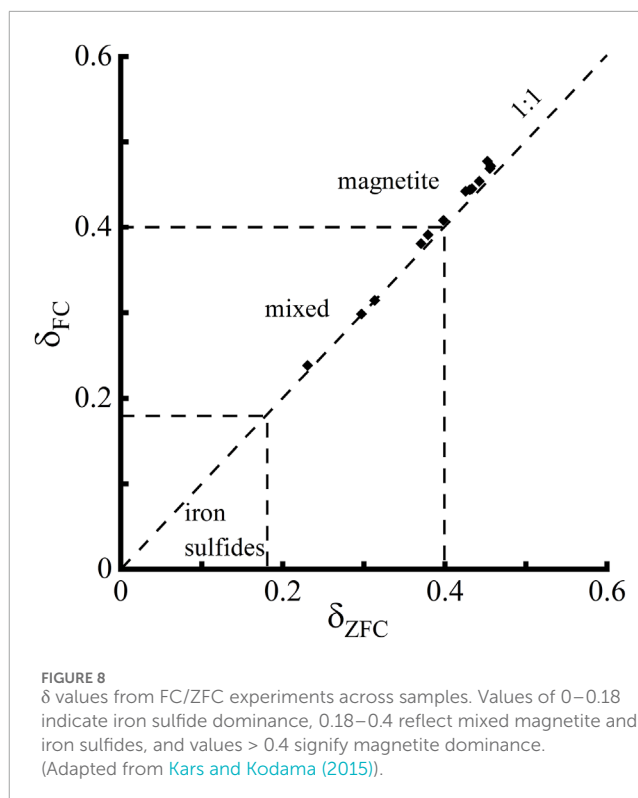
$$\delta = (J(80K) - J(150K))/J(80K) \qquad (5)$$

where J(T) represents remanence measured at temperature T after FC or ZFC treatment (Moskowitz et al., 1993). Fresh magnetotactic bacteria typically exhibit a δ_{FC}/δ_{ZFC} ratio >2; in contrast, our samples average ~1.03 (Table 2). This suppression primarily results from dominant SP particle signals overwhelming the Verwey transition - a documented interference mechanism that impedes magnetofossil identification via δ_{FC}/δ_{ZFC} ratios (Moskowitz et al., 1993; Housen and Moskowitz, 2006). The preservation mechanism for biogenic magnetite remains unresolved; however, its co-occurrence with magnetite inclusions has been documented in several studies (Chang et al., 2016b).

4.4 Diagenesis in gas hydrate-bearing sediments: Shallow vs. deep comparison

The LTC data comparisons reveal significantly higher saturation remanence (SIRM > $1E^{-3}Am^2$/kg) in shallow samples from the Hikurangi Margin (68–460 mbsf) and the Nankai Trough (70–110 mbsf) compared to our deeper samples. FC/ZFC curves exhibit similarly elevated characteristics, with SIRM values substantially exceeding those in most deep samples (Kars et al., 2021; Kars and Kodama, 2015). FC/ZFC curves exhibit similarly elevated characteristics, with SIRM values substantially exceeding those in most deep samples. Furthermore, these curves display comparatively enhanced Verwey transitions near 120 K relative to deeper sediments. A notable drop in remanence occurs at ~490 mbsf in the Hikurangi Margin. Furthermore, the δ parameter (δ_{FC} and δ_{ZFC}) quantifies the relative proportions of magnetite versus ferrimagnetic iron sulfides. Plotting δ values (Figure 8) shows most samples fall within the magnetite-dominant field. Only a discrete anomalous sample at ~605.8 mbsf plots within the mixed magnetite/iron sulfide field, resembling the magnetic composition of shallow Hikurangi Margin samples. This indicates that magnetite—despite its depleted concentrations—remains the predominant magnetic phase throughout most deep sediment sections. Greigite content variations align with D_{JH} data, showing low overall abundance of single-domain greigite grains, except at the discrete anomaly where it is higher. Collectively, comparison with low-temperature experimental data from shallow gas hydrate-bearing sediments reveals that deep burial sediments (>580 mbsf) exhibit: significantly depleted magnetic mineral concentrations, advanced reductive dissolution of magnetite, and pyritization progressing toward completion.

5 Conclusion

Compared to gas hydrate-bearing shallow sediments in other marine settings, magnetite in the deep anoxic sediments at Site U1519 has been nearly completely depleted by intense pyritization. Consequently, the magnetic assemblage is now dominated by SP grains (F_{SP} >90%), as evidenced by a prominent monotonic decay in the FC/ZFC curves. Within the reducing environment, the preservation of authigenic greigite is controlled by low sulfate concentrations and reactive iron concentrations. These conditions suppress microbial H_2S production and pyritization, allowing greigite to persist as an intermediate reaction product.

FIGURE 8
δ values from FC/ZFC experiments across samples. Values of $0-0.18$ indicate iron sulfide dominance, $0.18-0.4$ reflect mixed magnetite and iron sulfides, and values > 0.4 signify magnetite dominance. (Adapted from Kars and Kodama (2015)).

Furthermore, dual Verwey transition peaks (~106 K and ~118 K) in select samples indicate the coexistence of biogenic magnetite and inorganic magnetite. Suppression by SP particle signals resulted in low δ_{FC}/δ_{ZFC} ratios, complicating the identification of biogenic magnetite compared to fresh magnetosomes. Nevertheless, the presence of biogenic magnetite demonstrates its potential for preservation even within deep reducing settings, challenging the assumption of its inevitable dissolution. Collectively, this study demonstrates that low-temperature magnetism can be used to decipher the preservation and alteration of magnetic minerals, thereby providing a new magnetic perspective for understanding diagenetic evolution within gas hydrate systems of the Hikurangi margin.

Data availability statement

The data collected for this study can be found at https://doi.org/10.5281/zenodo.15639564. All Expedition 375 shipboard data are available at https://web.iodp.tamu.edu/OVERVIEW.

Author contributions

SL: Writing – original draft. XL: Writing – review and editing. KX: Writing – review and editing.

Funding

Acknowledgements

Conflict of interest

The author(s) declared that this work was conducted in the absence of any commercial or financial relationships that could be construed as a potential conflict of interest.

Generative AI statement

The author(s) declared that generative AI was not used in the creation of this manuscript.

Any alternative text (alt text) provided alongside figures in this article has been generated by Frontiers with the support of artificial intelligence and reasonable efforts have been made to ensure accuracy, including review by the authors wherever possible. If you identify any issues, please contact us.

Publisher's note

All claims expressed in this article are solely those of the authors and do not necessarily represent those of their affiliated organizations, or those of the publisher, the editors and the reviewers. Any product that may be evaluated in this article, or claim that may be made by its manufacturer, is not guaranteed or endorsed by the publisher.

References

Badesab, F, Dewangan, P., Gaikwad, V., Kars, M., Kocherla, M., Krishna, K. S., et al. (2019). Magnetic mineralogical approach for the exploration of gas hydrates in the Bay of Bengal. *J. Geophys. Res. Solid Earth* 124, 4428–4451. doi:10.1029/2019JB017466

Badesab, F, Gaikwad, V., and Dewangan, P. (2020). Controls on greigite preservation in a gas hydrate system of the krishna-godavari basin, Bay of Bengal. *Geo-Marine Lett.* 40, 439–452. doi:10.1007/s00367-019-00604-z

Badesab, F, Gaikwad, V., Venkateshwarlu, M., Kadam, N., and JoãO, H. M. (2022). Diagenetic dissolution, maghemitization and sulphidization of magnetic minerals in rapidly deposited gas hydrate bearing sediments from the Bay of Bengal. *Mar. Petroleum Geol.* 139, 105585. doi:10.1016/j.marpetgeo.2022.105585

Barnes, P., Wu, H. Y., Saffer, D., Pecher, I., Petronotis, K., LeVay, L., et al. (2019). "Site U1519," in *Hikurangi subduction margin coring, logging, and observatories*. Editors L. WALLACE, and S. THE EXPEDITION (College Station, TX: International Ocean Discovery Program), 372B/375. doi:10.14379/iodp.proc.372B375.104.2019

Bazylinski, D. A., Frankel, R. B., Garratt-Reed, A. J., and Mann, S. (1991). "Biomineralization of iron sulfides in magnetotactic bacteria from sulfidic environments," in *Iron biominerals*. Editors R. B. FRANKEL, and R. P. BLAKEMORE (Boston, MA: Springer US), 239–255. doi:10.1007/978-1-4615-3810-3_17

Chang, L., Winklhofer, M., Roberts, A. P., Heslop, D., Florindo, F., Dekkers, M. J., et al. (2013). Low-temperature magnetic properties of pelagic carbonates: oxidation of biogenic magnetite and identification of magnetosome chains. *J. Geophys. Res. Solid Earth* 118, 6049–6065. doi:10.1002/2013JB010381

Chang, L., Heslop, D., Roberts, A. P., Rey, D., and Mohamed, K. J. (2016a). Discrimination of biogenic and detrital magnetite through a double verwey transition temperature. *J. Geophys. Res. Solid Earth* 121, 3–14. doi:10.1002/2015JB012485

Chang, L., Roberts, A. P., Heslop, D., Hayashida, A., Li, J., Zhao, X., et al. (2016b). Widespread occurrence of silicate-hosted magnetic mineral inclusions in marine sediments and their contribution to paleomagnetic recording. *J. Geophys. Res. Solid Earth* 121, 8415–8431. doi:10.1002/2016JB013109

Dunlop, D. J. (2002). Theory and application of the day plot (Mrs/Ms versus hcr/Hc) 2. Application to data for rocks, sediments, and soils. *J. Geophys. Res. Solid Earth* 107 (EPM 5-1-), 5–15. doi:10.1029/2001JB000487

Frederichs, T., Von Dobeneck, T., Bleil, U., and Dekkers, M. J. (2003). Towards the identification of siderite, rhodochrosite, and vivianite in sediments by their low-temperature magnetic properties. *Phys. Chem. Earth, Parts A/B/C* 28, 669–679. doi:10.1016/S1474-7065(03)00121-9

Gaikwad, V., Badesab, F., Dewangan, P., and Kotha, M. (2021). Diagenesis of magnetic minerals in active/relict methane seep: constraints from rock magnetism and mineralogical records from Bay of Bengal. *Front. Earth Sci.* 9, 9–2021. doi:10.3389/feart.2021.638594

Gaikwad, V., Badesab, F., and Kotha, M. (2022). Diagenetic analysis of shallow and deep-seated gas hydrate systems from the Bay of Bengal. *Mar. Geol.* 449, 106824. doi:10.1016/j.margeo.2022.106824

Housen, B. A., and Moskowitz, B. M. (2006). Depth distribution of magnetofossils in near-surface sediments from the blake/bahama outer ridge, Western north Atlantic Ocean, determined by low-temperature magnetism. *J. Geophys. Res. Biogeosciences* 111. doi:10.1029/2005JG000068

Housen, B. A., and Musgrave, R. J. (1996). Rock-magnetic signature of gas hydrates in accretionary prism sediments. *Earth Planet. Sci. Lett.* 139, 509–519. doi:10.1016/0012-821X(95)00245-8

Kars, M., and Kodama, K. (2015). Authigenesis of magnetic minerals in gas hydrate-bearing sediments in the nankai trough, offshore Japan. *Geochem. Geophys. Geosystems* 16, 947–961. doi:10.1002/2014GC005614

Kars, M., Musgrave, R. J., Kodama, K., Jonas, A.-S., Bordiga, M., Ruebsam, W., et al. (2017). Impact of climate change on the magnetic mineral assemblage in marine sediments from Izu rear arc, NW Pacific Ocean, over the last 1Myr. *Palaeogeogr. Palaeoclimatol. Palaeoecol.* 480, 53–69. doi:10.1016/j.palaeo.2017.05.016

Kars, M., Musgrave, R. J., Hoshino, T., Jonas, A.-S., Bauersachs, T., Inagaki, F., et al. (2018). Magnetic mineral diagenesis in a high temperature and deep methanic zone in izu rear arc Marine sediments, Northwest Pacific Ocean. *J. Geophys. Res. Solid Earth* 123, 8331–8348. doi:10.1029/2018JB015861

Kars, M., Greve, A., and Zerbst, L. (2021). Authigenic greigite as an indicator of methane diffusion in gas hydrate-bearing sediments of the hikurangi margin, New Zealand. *Front. Earth Sci.* 9, 603363. doi:10.3389/feart.2021.603363

LarrasoañA, J. C., Roberts, A. P., Musgrave, R. J., GràCIA, E., PiñERO, E., Vega, M., et al. (2007). Diagenetic formation of greigite and pyrrhotite in gas hydrate marine sedimentary systems. *Earth Planet. Sci. Lett.* 261, 350–366. doi:10.1016/j.epsl.2007.06.032

Liu, Q., Yu, Y., Torrent, J., Roberts, A. P., Pan, Y., and Zhu, R. (2006). Characteristic low-temperature magnetic properties of aluminous goethite [α-(Fe, Al)OOH] explained. *J. Geophys. Res. Solid Earth* 111. doi:10.1029/2006JB004560

Liu, J., Shi, X., Liu, Q., Ge, S., Liu, Y., Yao, Z., et al. (2014). Magnetostratigraphy of a greigite-bearing core from the south yellow sea: implications for remagnetization and sedimentation. *J. Geophys. Res. Solid Earth* 119, 7425–7441. doi:10.1002/2014JB011206

Moskowitz, B. M., Frankel, R. B., and Bazylinski, D. A. (1993). Rock magnetic criteria for the detection of biogenic magnetite. *Earth Planet. Sci. Lett.* 120, 283–300. doi:10.1016/0012-821X(93)90245-5

Özdemir, Ö., and Dunlop, D. J. (2010). Hallmarks of maghemitization in low-temperature remanence cycling of partially oxidized magnetite nanoparticles. *J. Geophys. Res. Solid Earth* 115. doi:10.1029/2009JB006756

Özdemir, Ö., Dunlop, D. J., and Moskowitz, B. M. (2002). Changes in remanence, coercivity and domain state at low temperature in magnetite. doi:10.1016/S0012-821X(01)00562-3

Paterson, G. A., Zhao, X., Jackson, M., and Heslop, D. (2018). Measuring, processing, and analyzing hysteresis data. *Geochem. Geophys. Geosystems* 19, 1925–1945. doi:10.1029/2018GC007620

Pick, T., and Tauxe, L. (1994). Characteristics of magnetite in submarine basaltic glass. *Geophys. J. Int.* 119, 116–128. doi:10.1111/j.1365-246X.1994.tb00917.x

Qian, Y., Heslop, D., Roberts, A. P., Hu, P., Zhao, X., Liu, Y., et al. (2021). Low-temperature magnetic properties of marine sediments—quantifying magnetofossils, superparamagnetism, and maghemitization: Eastern mediterranean examples. *J. Geophys. Res. Solid Earth* 126, e2021JB021793. doi:10.1029/2021JB021793

Roberts, A. P. (1995). Magnetic properties of sedimentary greigite (Fe3S4). *Earth Planet. Sci. Lett.* 134, 227–236. doi:10.1016/0012-821X(95)00131-U

Roberts, A. P., Chang, L., Rowan, C. J., Horng, C.-S., and Florindo, F. (2011). Magnetic properties of sedimentary greigite (Fe3S4): an update. *Rev. Geophys.* 49. doi:10.1029/2010RG000336

Roberts, A. P., Chang, L., Heslop, D., Florindo, F., and LarrasoañA, J. C. (2012). Searching for single domain magnetite in the "pseudo-single-domain" sedimentary haystack: implications of biogenic magnetite preservation for sediment magnetism and relative paleointensity determinations. *J. Geophys. Res. Solid Earth* 117. doi:10.1029/2012JB009412

Rowan, C. J., and Roberts, A. P. (2006). Magnetite dissolution, diachronous greigite formation, and secondary magnetizations from pyrite oxidation: unravelling complex magnetizations in Neogene marine sediments from New Zealand. *Earth Planet. Sci. Lett.* 241, 119–137. doi:10.1016/j.epsl.2005.10.017

Saffer, D., Wu, H. Y., Barnes, P., Pecher, I., Petronotis, K., LeVay, L., et al. (2019). "Expedition 372B/375 summary," in *Hikurangi subduction margin coring, logging, and observatories. Proceedings of the international ocean discovery program*. Editors L. WALLACE, and S. THE EXPEDITION (College Station, TX: Proceedings of the International Ocean Discovery Program), 372B/375. doi:10.14379/iodp.proc.372b375.101.2019

Smirnov, A. V., and Tarduno, J. A. (2000). Low-temperature magnetic properties of pelagic sediments (ocean drilling program site 805C): tracers of maghemitization and magnetic mineral reduction. *J. Geophys. Res. Solid Earth* 105, 16457–16471. doi:10.1029/2000JB900140

Smith, P. P. K. (1979). The identification of single-domain titanomagnetite particles by means of transmission electron microscopy. *Can. J. Earth Sci.* 16, 375–379. doi:10.1139/e79-035

Tarduno, J. A. (1995). Superparamagnetism and reduction diagenesis in pelagic sediments: enhancement or depletion? *Geophys. Res. Lett.* 22, 1337–1340. doi:10.1029/95GL00888

Tauxe, L., Bertram, H. N., and Seberino, C. (2002). Physical interpretation of hysteresis loops: micromagnetic modeling of fine particle magnetite. *Geochem. Geophys. Geosystems* 3, 1–22. doi:10.1029/2001GC000241

Wallace, L. M., Saffer, D. M., Barnes, P. M., Pecher, I. A., Petronotis, K. E., LeVay, L. J., et al. (2019). Hikurangi subduction margin coring, logging, and observatories. *Proc. Int. Ocean Discov. Program* 372B/375. doi:10.14379/iodp.proc.372B375.2019

Wang, S., Chang, L., Wu, T., and Tao, C. (2020). Progressive dissolution of titanomagnetite in high-temperature hydrothermal vents dramatically reduces magnetization of basaltic ocean crust. *Geophys. Res. Lett.* 47, e2020GL087578. doi:10.1029/2020GL087578

Wang, S., Chang, L., Tao, C., Bilardello, D., Liu, L., and Wu, T. (2021). Seafloor magnetism under hydrothermal alteration: insights from magnetomineralogy and magnetic properties of the southwest Indian ridge basalts. *J. Geophys. Res. Solid Earth* 126, e2021JB022646. doi:10.1029/2021JB022646

Yang, H., Zhang, P., Lu, H., Shi, M., Li, J., Lu, Y., et al. (2023). Magnetic properties of gas hydrate-bearing sediments and their association with iron geochemistry in the Sea of Marmara, Turkey. *Chem. Geol.* 620, 121339. doi:10.1016/j.chemgeo.2023.121339